Topological phase transition and detectable edge state in a quasi-three-dimensional circuit quantum electrodynamic lattice

Kai-Xin Hu [1], Chao Chen,[1] Lu Qi,[2] Wen-Xue Cui,[1,*] Shou Zhang,[1] and Hong-Fu Wang [1,†]

[1]*Department of Physics, College of Science, Yanbian University, Yanji, Jilin 133002, China*
[2]*Department of Physics, Harbin Institute of Technology, Harbin, Heilongjiang 150001, China*

We investigate the topological phase transition and the edge states in a quasi-three-dimensional topological system mapped by a circuit quantum electrodynamic lattice via introducing two periodic spatial parameters. It is found that with the increasing of the periodically modulated on-site potential strength, the system undergoes a topological phase transition, corresponding to the change of the number of Weyl points under the periodic boundary condition. Under the open boundary condition, the phase transition is reflected by the energy band separation and the appearance of new edge states. Interestingly, the system holds two pairs of crossed edge states in the energy gaps when the periodic parameters take certain values. Furthermore, we show that, benefiting from the Bose statistical properties of the circuit quantum electrodynamic, the edge states of the system can be directly detected by measuring the average photon number of the cavity field in the steady state.

I. INTRODUCTION

The exploration of novel quantum phases, which is the central topic in condensed matter physics, has attracted extensive interest in recent decades [1–6]. Especially, topological insulators have attracted much attention due to the existence of novel physical phenomena. The electronic band structure of the topological insulator is similar to the traditional insulator, in which the Fermi energy level lies between the conduction and valence band [7–10]. However, the difference is that the topological insulator possesses a localized conducting surface state or edge state existing in the band gap, which can support the unidirectional transmission against backscatter [4,11–13]. This special band structure can be actually determined by the topological properties of materials [14,15]. For instance, the Majorana fermions show the non-Abelian statistics, which has potential applications in topological quantum computing [16,17]. Note that, under natural conditions, the original static systems with topological properties are awfully limited, which inspires the researchers to artificially change the structures and properties of materials to realize the mapping of topological insulators based on various kinds of physical platforms [18,19].

Recently, with the rapid development of micro- and nano-processing technology, circuit quantum electrodynamics (QED) has become one of the important physical platforms for implementing quantum information processing, topological quantum computing, and quantum simulation. Compared with other quantum systems, the circuit QED system composed of superconducting quantum bits and microwave cavity fields is easily integrated in space and modulated in time, which provides structural designability and parameter adjustability

simultaneously [20–22]. On the other hand, superconducting qubits possess discrete energy levels which can be modulated through external fields, and their coherence time has also been improved greatly by using current technology. Typically, the Xmon superconducting qubit, which can be regarded as a nonlinear harmonic oscillator, in which the lowest two energy levels are chosen as qubits [23], can be coupled with the coplanar waveguide resonator and the transmission line in one-dimensional (1D) space [24]. When the superconducting qubits as artificial atoms are coupled to the transmission line resonators, a series of experimental studies on microwave quantum optics can be realized due to their convenient coupling modulations [25]. Taking advantage of the high integration in space and the flexible modulation in time of the circuit QED, one can design and investigate more complex multibody quantum effects and quantum simulation of topological insulators [26–28]. So far, the phase transition and the edge state of topological insulators have been widely studied both in theory and in experiments [29–31]. And a scheme has been proposed to study the topological phases of higher-dimensional systems by using quasicrystals [32]. It is of great importance to find experimentally feasible 3D materials with observable bulk band gaps to solve the bottleneck of the development of 3D topological insulators [33–36]. In view of the advantages of circuit QED systems in structure designability and parameter adjustability, circuit QED lattice systems can provide the possibility and feasibility for mapping high-dimensional topological systems accurately. Furthermore, due to the property of Bose statistics of circuit QED, the topological invariant and edge state of the system can be detected by utilizing the lattice-based cavity input-output process [21].

In this paper, motivated by the above, we propose a simple and feasible method to realize the mapping from a 1D to a 3D topological system by introducing two periodic spatial dimensions in a circuit QED lattice system. Under the

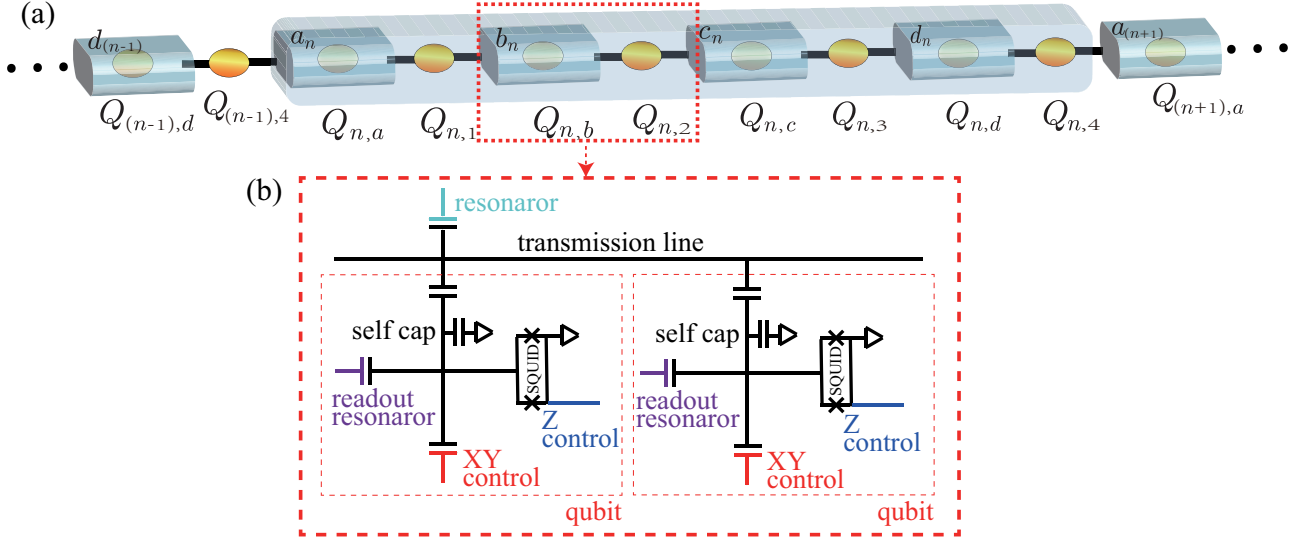*cuiwenxue@ybu.edu.cn
†hfwang@ybu.edu.cn

FIG. 1. (a) Schematic diagram of the circuit QED lattice. The resonators are labeled as a_n, b_n, c_n, and d_n and the two adjacent resonators are connected by qubits $Q_{n,1}$, $Q_{n,2}$, $Q_{n,3}$, and $Q_{n,4}$. Each resonator a_n (b_n, c_n, d_n) is coupled to a two-level Xmon qubit $Q_{n,a}$ ($Q_{n,b}$, $Q_{n,c}$, $Q_{n,d}$), and the box in the shadow area defines the unit cell of the circuit QED lattice. (b) Circuit structure diagrams. The qubits can be easily read out via the coplanar waveguide resonators and controlled via the control lines (*XY* control and *Z* control), and the coupling between the resonators and the qubits can be realized by a capacitance.

periodic boundary condition (PBC) and the open boundary condition (OBC), we explore the effects of periodic on-site potential strength and periodic parameters on the topological phase transition and the edge state by calculating the energy spectrum of the system, respectively. In the case of the PBC, it is shown that the number of Weyl points at $E - \Delta_e = 0$ changes from zero to four with the increasing of the periodic potential strength V, which corresponds to a topological phase transition with critical value $V = \sqrt{2}$. While for the OBC, the system possesses four energy bands and three energy gaps for a mild potential strength V, and then the upper two energy bands and the lower two energy bands separate from each other. Meanwhile, two new edge states appear in the second energy gap. Interestingly, crossed edge states respectively appear in the first and third energy gaps of the energy spectrum when the periodic parameters take certain values. Moreover, by using the lattice-based cavity input-output process, the edge states can be directly detected by measuring the average photon number of the cavity field in the steady state.

The rest of the paper is organized as follows. In Sec. II, we present the model and the Hamiltonian of the system. In Sec. III, we analyze the energy spectrum of the system under the PBC and the OBC. Also, we give the method for detecting the edge states by using the lattice-based cavity input-output process. Finally, a conclusion is given in Sec. IV.

II. MODEL AND HAMILTONIAN

We consider a 1D circuit QED lattice system, as shown in Fig. 1, where each unit cell contains four resonators and eight two-level superconducting Xmon qubits, respectively. Here each Xmon qubit has one excited state $|e\rangle$ and one ground state $|g\rangle$. In the *n*th unit cell, the resonators a_n (b_n, c_n, d_n) and b_n (c_n, d_n, a_{n+1}) are coupled to the Xmon qubit $Q_{n,1}$ ($Q_{n,2}$, $Q_{n,3}$, $Q_{n,4}$). At the same time, the Xmon qubit labeled

by $Q_{n,a}$ ($Q_{n,b}$, $Q_{n,c}$, $Q_{n,d}$) is embedded into each resonator a_n (b_n, c_n, d_n) to provide additional control on the resonator. The Hamiltonian of the circuit QED lattice system is written as

$$
H_1 = \sum_n \left\{ \sum_i \frac{\omega_i}{2} \sigma_{ni}^z + \omega_e (a_n^\dagger a_n + b_n^\dagger b_n + c_n^\dagger c_n + d_n^\dagger d_n) \right.
$$
$$
+ \left[g_1 \sigma_{n1}^+ (a_n + b_n) + g_2 \sigma_{n2}^+ (b_n + c_n) + g_a \sigma_{na}^+ a_n \right.
$$
$$
+ g_3 \sigma_{n3}^+ (c_n + d_n) + g_4 \sigma_{n4}^+ (d_n + a_{n+1}) + g_b \sigma_{nb}^+ b_n
$$
$$
\left. \left. + g_c \sigma_{nc}^+ c_n + g_d \sigma_{nd}^+ d_n + \text{H.c.} \right] \right\}, \tag{1}
$$

where ω_i ($i = 1, 2, 3, 4, a, b, c, d$) is the frequency of the eight Xmon qubits $Q_{n,i}$, ω_e is the frequency of the four resonators, g_1 (g_2, g_3, g_4) is the coupling strength between the Xmon qubit $Q_{n,1}$ ($Q_{n,2}$, $Q_{n,3}$, $Q_{n,4}$) and the resonators a_n (b_n, c_n, d_n) and b_n (c_n, d_n, a_{n+1}), and g_a (g_b, g_c, g_d) is the coupling strength between the resonator a_n (b_n, c_n, d_n) and the Xmon qubit $Q_{n,a}$ ($Q_{n,b}$, $Q_{n,c}$, $Q_{n,d}$). $\sigma_{ni}^z = |e\rangle\langle e| - |g\rangle\langle g|$, $\sigma_{ni}^+ = |e\rangle\langle g|$, and $\sigma_{ni}^- = |g\rangle\langle e|$ ($i = 1, 2, 3, 4, a, b, c, d$) represent the atomic population operator, the raising operator, and the lowering operator of the Xmon qubit, respectively.

In the rotating frame, with respect to the external driving frequency ω_f and the qubit frequency ω_i ($i = 1, 2, 3, 4, a, b, c, d$) where all the Xmon qubits are prepared in the ground states, the effective Hamiltonian of the system can be written as

$$
H_2 = \sum_n \left[\left(\Delta_e - \frac{g_4^2}{\Delta_4} - \frac{g_1^2}{\Delta_1} - \frac{g_a^2}{\Delta_a} \right) a_n^\dagger a_n - \frac{g_1^2}{\Delta_1} a_n^\dagger b_n \right.
$$
$$
+ \left(\Delta_e - \frac{g_1^2}{\Delta_1} - \frac{g_2^2}{\Delta_2} - \frac{g_b^2}{\Delta_b} \right) b_n^\dagger b_n - \frac{g_4^2}{\Delta_4} d_n a_{n+1}^\dagger
$$

$$+ \left(\Delta_e - \frac{g_2^2}{\Delta_2} - \frac{g_3^2}{\Delta_3} - \frac{g_c^2}{\Delta_c} \right) c_n^\dagger c_n - \frac{g_4^2}{\Delta_4} d_n^\dagger a_{n+1}$$

$$+ \left(\Delta_e - \frac{g_3^2}{\Delta_3} - \frac{g_4^2}{\Delta_4} - \frac{g_d^2}{\Delta_d} \right) d_n^\dagger d_n - \frac{g_1^2}{\Delta_1} a_n b_n^\dagger$$

$$- \frac{g_2^2}{\Delta_2} b_n c_n^\dagger - \frac{g_2^2}{\Delta_2} b_n^\dagger c_n - \frac{g_3^2}{\Delta_3} c_n^\dagger d_n - \frac{g_3^2}{\Delta_3} c_n d_n^\dagger \Bigg], \quad (2)$$

where $\Delta_i = \omega_i - \omega_e$ ($i = 1, 2, 3, 4, a, b, c, d$) is the detuning of the qubits $Q_{n,i}$, $\Delta_e = \omega_e - \omega_f$ is the detuning of the resonators, g_1 (g_2, g_3, g_4) is the coupling strength between the Xmon qubit $Q_{n,1}$ ($Q_{n,2}$, $Q_{n,3}$, $Q_{n,4}$) and the resonators a_n (b_n, c_n, d_n) and b_n (c_n, d_n, a_{n+1}), and g_a (g_b, g_c, g_d) is the coupling strength between the resonator a_n (b_n, c_n, d_n) and the Xmon qubit $Q_{n,a}$ ($Q_{n,b}$, $Q_{n,c}$, $Q_{n,d}$). Equation (2) contains the on-site energy and the nearest-neighboring interaction. The detailed derivation of Eq. (2) is shown in Appendix A.

Here, we set the photon hopping strengths between the resonators as $-\frac{g_1^2}{\Delta_1} = -\frac{g_3^2}{\Delta_3} = \cos\varphi$ and $-\frac{g_2^2}{\Delta_2} = -\frac{g_4^2}{\Delta_4} = \sin\varphi$, and we set the coupling strengths between the resonators and the Xmon qubits as $g_a^2 = \Delta_a(-\frac{g_4^2}{\Delta_4} - \frac{g_1^2}{\Delta_1} + V\sin\theta)$, $g_b^2 = \Delta_b(-\frac{g_1^2}{\Delta_1} - \frac{g_2^2}{\Delta_2} + V\cos\theta)$, $g_c^2 = \Delta_c(-\frac{g_2^2}{\Delta_2} - \frac{g_3^2}{\Delta_3} - V\sin\theta)$, and $g_d^2 = \Delta_d(-\frac{g_3^2}{\Delta_3} - \frac{g_4^2}{\Delta_4} - V\cos\theta)$. Then, the Hamiltonian in Eq. (2) can be rewritten as

$$H = \sum_n [(\Delta_e - V\sin\theta) a_n^\dagger a_n + (\Delta_e - V\cos\theta) b_n^\dagger b_n$$
$$+ (\Delta_e + V\sin\theta) c_n^\dagger c_n + (\Delta_e + V\cos\theta) d_n^\dagger d_n$$
$$+ (\cos\varphi\, a_n^\dagger b_n + \sin\varphi\, b_n^\dagger c_n + \cos\varphi\, c_n^\dagger d_n$$
$$+ \sin\varphi\, d_n^\dagger a_{n+1} + \text{H.c.})]. \quad (3)$$

Obviously, the above Hamiltonian is equivalent to a four-band topological model with both the on-site modulation and nearest-neighboring hopping modulation.

To further explore the topological properties of the circuit QED lattice model, we introduce the Fourier transform $\hat{\beta}_n = \frac{1}{\sqrt{L_x}} \sum_{k_x} e^{itnk_x} \hat{\beta}_{k_x}$ ($\hat{\beta}_n = a_n, b_n, c_n, d_n$), with $t = 1$ being the lattice constant and k_x being the wave vector defined in the Brillouin region. Then the Hamiltonian in momentum space can be expressed as

$$H(\mathbf{k}) = \sum_{\mathbf{k}} [(\Delta_e - V\sin\theta) \hat{a}_{\mathbf{k}}^\dagger \hat{a}_{\mathbf{k}} + (\Delta_e - V\cos\theta) \hat{b}_{\mathbf{k}}^\dagger \hat{b}_{\mathbf{k}}$$
$$+ (\Delta_e + V\sin\theta) \hat{c}_{\mathbf{k}}^\dagger \hat{c}_{\mathbf{k}} + (\Delta_e + V\cos\theta) \hat{d}_{\mathbf{k}}^\dagger \hat{d}_{\mathbf{k}}$$
$$+ (e^{ik_x} \cos\varphi\, \hat{a}_{\mathbf{k}}^\dagger \hat{b}_{\mathbf{k}} + e^{ik_x} \sin\varphi\, \hat{b}_{\mathbf{k}}^\dagger \hat{c}_{\mathbf{k}}$$
$$+ e^{ik_x} \cos\varphi\, \hat{c}_{\mathbf{k}}^\dagger \hat{d}_{\mathbf{k}} + e^{ik_x} \sin\varphi\, \hat{d}_{\mathbf{k}}^\dagger \hat{a}_{\mathbf{k}} + \text{H.c.})]. \quad (4)$$

For convenience, we rewrite the above Hamiltonian as

$$H(\mathbf{k}) = \hat{\psi}_{\mathbf{k}}^\dagger h(\mathbf{k}) \hat{\psi}_{\mathbf{k}}, \quad (5)$$

where $\hat{\psi}_{\mathbf{k}} = (\hat{a}_{\mathbf{k}}, \hat{b}_{\mathbf{k}}, \hat{c}_{\mathbf{k}}, \hat{d}_{\mathbf{k}})^T$ and $h(\mathbf{k})$ is the Hamiltonian density, with

$$\begin{bmatrix} \Delta_e - V\sin\theta & e^{ik_x}\cos\varphi & 0 & e^{-ik_x}\sin\varphi \\ e^{-ik_x}\cos\varphi & \Delta_e - V\cos\theta & e^{ik_x}\sin\varphi & 0 \\ 0 & e^{-ik_x}\sin\varphi & \Delta_e + V\sin\theta & e^{ik_x}\cos\varphi \\ e^{ik_x}\sin\varphi & 0 & e^{-ik_x}\cos\varphi & \Delta_e + V\cos\theta \end{bmatrix}.$$
$$(6)$$

The Hamiltonian is a number of symmetry class AIII in the Altland-Zirnbauer symmetry classes, it does not satisfy the time-inversion symmetry or particle-hole symmetry, but only satisfies the chiral symmetry $Sh(\mathbf{k})S^{-1} = -h(\mathbf{k})$, with

$$S = \begin{bmatrix} 0 & 0 & 1 & 0 \\ 0 & 0 & 0 & -1 \\ 1 & 0 & 0 & 0 \\ 0 & -1 & 0 & 0 \end{bmatrix}. \quad (7)$$

The chiral symmetry ensures that the energy eigenvalues appear in pairs, which can be examined by diagonalizing Eq. (6), in which the energy dispersion spectrum can be easily obtained, with

$$E - \Delta_e = \pm \left[1 + \frac{V^2}{2} \pm \left(\cos^2 2k_x \sin^2 2\varphi + V^2 \right. \right.$$
$$\left. \left. + V^2 \cos 2\varphi \sin 2\theta + \frac{V^4}{4} \cos^2 2\theta \right)^{\frac{1}{2}} \right]^{\frac{1}{2}}. \quad (8)$$

Obviously, the energy dispersion spectrum indicates that the present system indeed contains two pairs of energy eigenvalues, which is consistent with the symmetry analysis. Besides, we find that the energy eigenvalue is closely related to the potential strength V. In the following, we investigate the effects of the potential strength V on the phase transition and the edge states of the system.

III. PHASE TRANSITION OF THE SYSTEM AND THE DETECTION OF EDGE STATES

To explore the phase transition of the system [37], we first consider the closing condition of energy gaps, i.e., $E - \Delta_e = 0$. The zero points of the dispersion are determined by

$$V^2 = \frac{2(\cos 2\varphi \pm i \sin 2\varphi \sin 2k_x)}{\sin 2\theta}. \quad (9)$$

From Eq. (9), equation $V^2 \sin(2\theta) = 2(\cos 2\varphi \pm i \sin 2\varphi)$ can be obtained when $k_x = p\pi/4$, with $p \in \mathbb{Z}$. If the potential strength is purely real, we can get the new equation $V^2 \sin 2\theta = \pm 2$ when $\varphi = p\pi/2$, with $p \in \mathbb{Z}$. The closing condition of energy gaps satisfies $V^2 \sin 2\theta \in [-2, 2]$. We can see that V^2 has a minimum critical value when $\sin 2\theta = \pm 1$, with $\theta = (p + \frac{1}{4})\pi$, $p \in \mathbb{Z}$. So the critical point of energy gap closing and reopening is $V^2 = 2$. When $V^2 < 2$, there is no energy gap closing in the system. In the following we choose $k_x = \pi/4$ in the first Brillouin zone.

To further investigate the topological phase transition, we plot the energy spectrum as a function of the periodic parameters φ and θ under the PBC for fixing $k_x = \pi/4$ with $V = 1$, $\sqrt{2}$, and 2, respectively, as shown in Fig. 2. For $V < \sqrt{2}$, there are no Weyl points existing in the system at $E - \Delta_e = 0$, as shown in Figs. 2(a) and 2(b). Figures 2(c) and 2(d) show that the system holds two Weyl points at $E - \Delta_e = 0$ with $V = \sqrt{2}$. For $V > \sqrt{2}$, two original Weyl points separate into four Weyl points at $E - \Delta_e = 0$, as shown in Figs. 2(e) and 2(f). The energy spectrum of the system changes obviously with the increasing of the potential strength V, which indicates that the system undergoes a topological phase transition at the critical point $V = \sqrt{2}$.
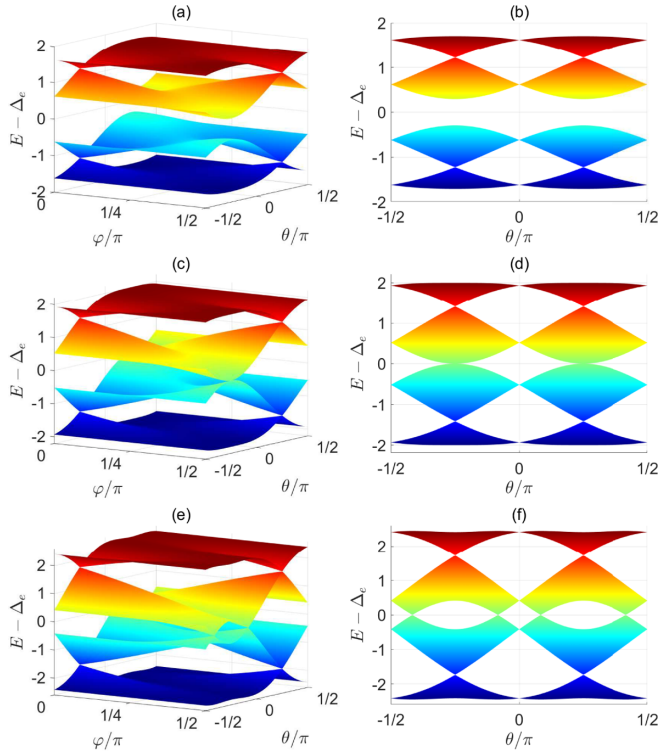
FIG. 2. Energy spectrum of the system as a function of the periodic parameters φ and θ with $k_x = \pi/4$ under the PBC, with the potential strengths (a) $V = 1$, (c) $V = \sqrt{2}$, and (e) $V = 2$. Here panels (b), (d), and (f) correspond to the main views of panels (a), (c), and (e), respectively.

FIG. 3. The energy spectrum as a function of the periodic parameters φ under the OBC, and the distribution of the edge state. The size of the lattice is $N = 40$, the periodic parameter is $\theta = \pi/4$, and the potential strengths are (a) $V = 1$, (c) $V = \sqrt{2}$, and (e) $V = 2$, respectively. The red solid and dashed lines represent the left edge states and the blue dotted and dash dotted lines represent the right edge states. (b), (d), and (f) are the state distributions of the left edge states marked by the red dashed line in (a), (c), and (e), respectively.

As we all know, there are no edge states existing in the energy gap for a topologically trivial insulator [38,39]. When the energy gap closes and reopens, the system is accompanied with a topological phase transition, i.e., from the topologically trivial phase to the topologically nontrivial phase. In the following, we adopt an open boundary condition along the x direction and plot the energy spectrum as a function of the periodic parameter φ with $V = 1$, $\sqrt{2}$, and 2, respectively, as shown in Fig. 3.

In Figs. 3(a), 3(c), and 3(e), the energy spectrum has four energy bands and three energy gaps, which are named in order from top to bottom, for example, the first energy gap, the first energy band, etc. The left and right edge states are represented by the red solid and dashed lines and the blue dotted and dash dotted lines, respectively. For $V = 1$ in Fig. 3(a), the first and third energy gaps of the system hold one edge state marked by the blue dash dotted and red solid lines, respectively, and the second energy gap holds two edge states marked by the red dashed and blue dash dotted lines, respectively. For $V = \sqrt{2}$ in Fig. 3(c), in comparison with Fig. 3(a), one can see that the second energy gap of the system closes. For $V = 2$ in Fig. 3(e), in comparison with Fig. 3(c), one can see that the second energy gap of the system reopens, and the second and third energy bands become two separated energy bands. Besides, comparing Figs. 3(a), 3(c), and 3(e), we note that the increasing of the potential strength V has a slight effect on the two edge states in the first and third energy gaps, respectively. We also plot the state distribution to present the localization of
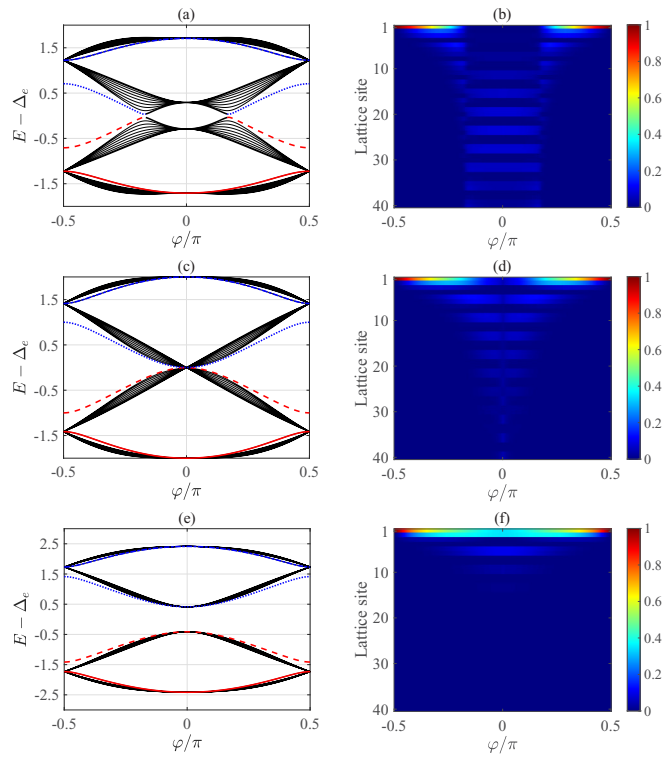
the edge states in Figs. 3(b), 3(d), and 3(f). Since the energy spectrum is symmetric with respect to $E - \Delta_e = 0$, we only draw one of the two edge states in the second energy gap. Figures 3(b), 3(d), and 3(f) are the state distributions of the left edge states which are marked by the red dashed line in Figs. 3(a), 3(c), and 3(e), respectively. Comparing Figs. 3(b), 3(d), and 3(f), one can see that the edge states in the second energy gap become more localized at both the ends of the lattice with the increasing of the potential strength V.

Then, we investigate the effect of the periodic parameter θ and the potential strength V on the edge states of the system. We plot the energy spectrum as a function of θ under the open boundary condition of the x direction, as shown in Fig. 4. In Figs. 4(a), 4(b), and 4(c), the system always has four edge states for different potential strengths V. When $\theta = -\pi/4$, two edge states cross in the first energy gap, which correspond to the left and right edge states marked by the red and blue lines, respectively. When $\theta = 3\pi/4$, another two edge states cross in the third energy gap, which correspond to the left and right edge states marked by the red solid and blue dotted lines, respectively. We find that no matter how the potential strength V changes, the edge states crossing are always at $\theta = -\pi/4$ and $\theta = 3\pi/4$. Comparing Figs. 4(a), 4(b), and 4(c), one can see that the crossing of edge states is robust to the variation
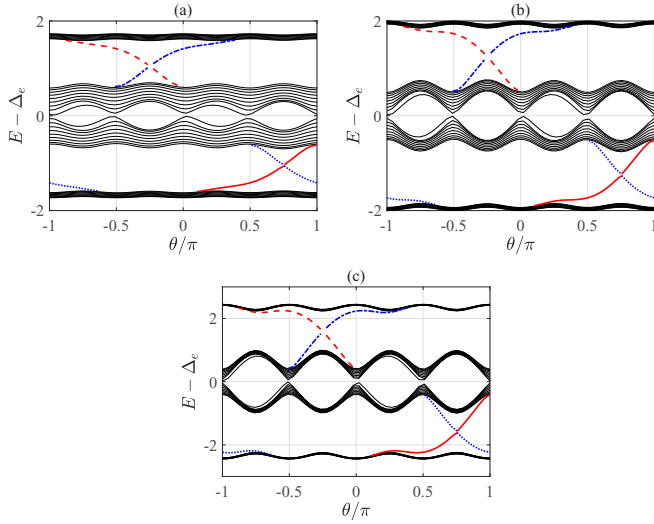
FIG. 4. The energy spectrum as a function of the periodic spatial parameter θ under the OBC with the different potential strength (a) $V = 1$, (b) $V = \sqrt{2}$, and (c) $V = 2$. In both cases, the size of the lattice $N = 40$, the other periodic spatial parameter $\varphi = \pi/4$, the red solid and dashed lines and the blue dotted and dash dotted lines represent the left edge states and the right edge states, respectively.

of the potential strength V, and the bulk energy bands become more compact with the increasing of the potential strength V.

On the basis of the above analysis, in Fig. 5, we further plot the state distributions of the four edge states of Fig. 4(c). The physical significance of the maximum state distribution at the lattice site is the position of the edge states in the whole system. Without loss of generality, the 1st lattice site is called the leftmost lattice site and the 40th lattice site is called the rightmost lattice site. For Fig. 5(a), in the regime of $\theta \in [-\pi, 0]$, one can see that the maximal state distribution appears at the leftmost lattice site, which corresponds to the
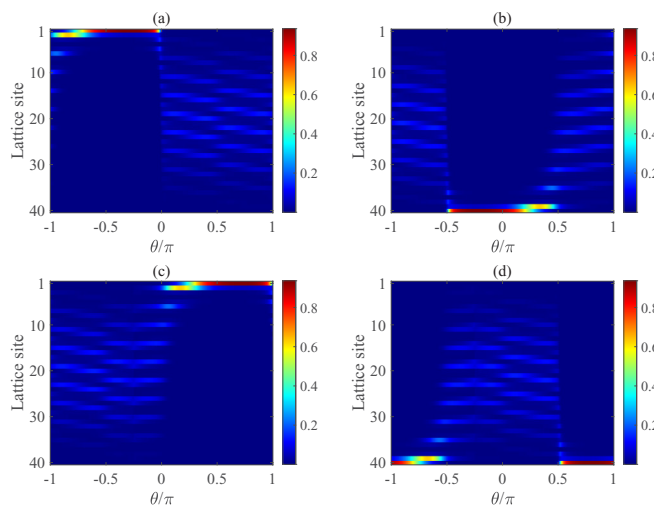

FIG. 5. The distribution of the edge states versus the periodic spatial parameter θ and the lattice site. The size of the latitce is $N = 40$, the periodic spatial parameter is $\varphi = \pi/4$, and the potential strength is $V = 2$. Panels (a) and (c) represent the distributions of the left edge states, and panels (b) and (d) represent the distributions of the right edge states.

left edge state marked by red dashed line in Fig. 4(c). In the regime of $\theta \in [-\pi/2, \pi/2]$ of Fig. 5(b), it is obvious that the maximal state distribution appears at the rightmost lattice site, which corresponds to the right edge state marked by blue dash dotted line in Fig. 4(c). For Figs. 5(c) and 5(d), we also show the state distributions of the left and right edge states marked by the red solid and blue dotted lines in Fig. 4(c). The maximal state distributions appear at the leftmost and rightmost lattice sites, which correspond to the regimes of $\theta \in [0, \pi]$ and $\theta \in [-\pi, -\pi/2] \cup [\pi/2, \pi]$, respectively.

It is known that the circuit QED lattice belongs to the boson system, in which the corresponding Bose photons in the resonators can occupy particular eigenstates simultaneously with different weights. Utilized by the lattice-based cavity input-output process, we can detect the edge states of the system directly [21]. Adjusting the frequency of the externally driven field to occupy the eigenenergy of the lattice, the driven Hamiltonian in the rotating frame with respect to the driving frequency ω_f is described as $H_d = \sum_n \{\Omega_{na} a_n^\dagger + \Omega_{nb} b_n^\dagger + \Omega_{nc} c_n^\dagger + \Omega_{nd} d_n^\dagger + \text{H.c.}\}$, where Ω_{na}, Ω_{nb}, Ω_{nc}, and Ω_{nd} are the driven amplitudes of the resonators a_n, b_n, c_n, and d_n in the nth unit cell. We solve the Lindblad master equation $\langle \dot{\rho}_j \rangle = -i\langle [H + H_d, \rho_j] \rangle + \kappa \langle L[\rho_n]\rho_j \rangle$, in which the Lindblad term is $L[\rho_n]\rho_j = \rho_n \rho_j \rho_n^\dagger - \{\rho_n^\dagger \rho_n, \rho_j\}/2$ and κ is the cavity decay rate. By taking the cavity dissipation into account, under the steady-state solution $\langle \dot{\rho}_j \rangle = 0$, we can get the expectation value of the cavity fields,

$$\vec{\rho} = -\left(\Delta_e + \vec{T}_{4n,4n} - i\frac{\kappa}{2}\right)^{-1}\vec{\Omega}, \tag{9}$$

where $\vec{\rho} = (\langle a_1 \rangle, \langle b_1 \rangle, \langle c_1 \rangle, \langle d_1 \rangle, \dots, \langle a_n \rangle, \langle b_n \rangle, \langle c_n \rangle, \langle d_n \rangle)^T$ is the final steady cavity field and $\vec{\Omega} = (\Omega_{1a}, \Omega_{1b}, \Omega_{1c}, \Omega_{1d}, \dots, \Omega_{na}, \Omega_{nb}, (\Omega_{nc}, \Omega_{nd})^T$ describes the driving amplitude, with T representing the transpose of the matrix. More details about the matrix $\vec{T}_{4n,4n}$ can be found in Appendix B.

In the following, we show how to detect the edge states. We first adjust the driving frequency ω_f that makes the Δ_e equal to the in-gap energy E, and then we select the $(4n \times 1)$ driven microwave pulses as $\vec{\Omega} = (\Omega_1, 0, 0, 0, \dots, 0, 0, 0, 0)^T$ to drive the leftmost resonator; after that the left edge state will be excited. In Fig. 6(a), we plot the average photon number of the cavity field in the steady state with $E = 1.82$, $\theta = -0.3066\pi$, and $\varphi = \frac{\pi}{4}$. We find that most of the photons are located on the leftmost resonator, which corresponds to the left edge state occupying the 1st resonator. Due to the nonresonance interaction, when the similarly driven microwave pulse with $[\vec{\Omega} = (0, 0, \dots, 0, \Omega_{21}, 0, \dots, 0, 0)^T]$ ($[\vec{\Omega} = (0, 0, \dots, 0, 0, 0, \dots, 0, \Omega_{40})^T]$) is used to drive the resonators, the photon distribution in the middle(rightmost) resonator is much smaller than that in the leftmost resonator. In Fig. 6(b), we detect the right edge state by using the same measurement method. It is shown that the maximal average photon number of the cavity field is at the 40th resonator, i.e., most of the photons are located on the rightmost resonator, which corresponds to the right edge state occupying the 40th resonator. In this way, we realize the detection of the edge states by measuring the average photon number based on the cavity input-output process in the steady state.
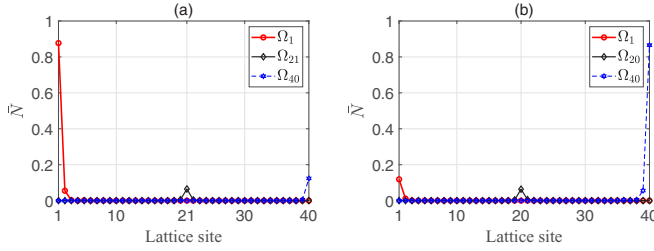
FIG. 6. Average photon number in the steady state when the left edge state and the right edge state are driven to be occupied by tuning (a) $\Delta_e = 1.82$ and (b) $\Delta_e = 1.323$. In both panels (a) and (b), the red circle, black diamond, and blue five-pointed star lines represent the leftmost, the middle, and the rightmost driven resonators, respectively. The size of the lattice is $N = 40$, the periodic spatial parameters are $\varphi = \pi/4$ and $\theta = -0.30663\pi$, the cavity dissipation rate is $\kappa = 0.2$, and the driving amplitudes are $\Omega_1 = \Omega_{20} = \Omega_{21} = \Omega_{40} = 0.2$.

IV. CONCLUSIONS AND DISCUSSIONS

In conclusion, we have proposed a simple and feasible scheme to realize the mapping from a 1D to a 3D topological system by introducing two periodic spatial parameters in a 1D circuit QED lattice. We investigate the effects of these spatial parameters on the topological phase transition and edge states of the system. It is shown that the system undergoes a topological phase transition induced by the increasing of the potential strength under the PBC. When the potential strength exceeds the critical value, we find that the number of Weyl points of the energy spectrum changes from zero to four. From the perspective of the OBC, with the increasing of the potential strength, the upper two energy bands and the lower two energy bands of the energy spectrum gradually separate from each other, and then the system holds two new edge states existing in the second energy gap. What is more interesting is that two pairs of the crossed edge states can be obtained by choosing certain periodic parameters, which are located in the first and third energy gaps, respectively. Moreover, taking advantage of the Bose statistical properties of the circuit QED, we realize the detection of the topological edge states via the lattice-based cavity input-output process in the steady state.

Our scheme provides a different and promising mechanism for exploring the topological properties by resorting to the quantum optical platform. The adjustability of the parameters for the circuit QED system ensures that we can introduce two or even much more additional periodic parameters and design the corresponding coupling coefficients to realize the mapping between the 1D circuit QED model and other high-dimensional topological models. The concept of synthetic dimension provides a pathway toward exploring higher-dimension physics.

APPENDIX A: THE EFFECTIVE HAMILTONIAN OF THE SYSTEM

Here we show the detailed derivation of Eq. (2). The Hamiltonian of the circuit QED lattice system is shown in Eq. (1), and then we define the following rotating transformation:

$$U = \exp\left\{-i\left[\sum_i \frac{\omega_i}{2}\sigma_{ni}^z + \omega_f(a_n^\dagger a_n + b_n^\dagger b_n + c_n^\dagger c_n + d_n^\dagger d_n)\right]t\right\}. \tag{A1}$$

In the rotating frame of Eq. (A1), the transformed Hamiltonian is given by

$$
\begin{aligned}
H_1^I = \sum_n \{ &\Delta_e(a_n^\dagger a_n + b_n^\dagger b_n + c_n^\dagger c_n + d_n^\dagger d_n) \\
&+ [g_1\sigma_{n1}^\dagger e^{i\Delta_1 t}(a_n + b_n) + g_a\sigma_{na}^\dagger e^{i\Delta_a t}a_n \\
&+ g_2\sigma_{n2}^\dagger e^{i\Delta_2 t}(b_n + c_n) + g_b\sigma_{nb}^\dagger e^{i\Delta_b t}b_n \\
&+ g_3\sigma_{n3}^\dagger e^{i\Delta_3 t}(c_n + d_n) + g_c\sigma_{nc}^\dagger e^{i\Delta_c t}c_n \\
&+ g_4\sigma_{n4}^\dagger e^{i\Delta_4 t}(d_n + a_{n+1}) + g_d\sigma_{nd}^\dagger e^{i\Delta_d t}d_n + \text{H.c.}]\},
\end{aligned}
\tag{A3}
$$

where $\Delta_e = \omega_e - \omega_f$ and $\Delta_i = \omega_i - \omega_f$ are the detunings of the resonators and Xmon qubits with respect to the external driving laser frequency, respectively.

In the case of the large detuning regime, the effective Hamiltonian of the system can be obtained as

$$
\begin{aligned}
H_{\text{eff}} = \sum_n [&\Delta_e(a_n^\dagger a_n + b_n^\dagger b_n + c_n^\dagger c_n + d_n^\dagger d_n) \\
&+ \frac{g_1^2}{\Delta_1}|e\rangle_{n_1}\langle e|(a_n a_n^\dagger + a_n b_n^\dagger + b_n a_n^\dagger + b_n b_n^\dagger) \\
&- \frac{g_1^2}{\Delta_1}|g\rangle_{n_1}\langle g|(a_n^\dagger a_n + b_n^\dagger a_n + a_n^\dagger b_n + b_n^\dagger b_n) \\
&+ \frac{g_2^2}{\Delta_2}|e\rangle_{n_2}\langle e|(b_n b_n^\dagger + b_n c_n^\dagger + c_n b_n^\dagger + c_n c_n^\dagger) \\
&- \frac{g_2^2}{\Delta_2}|g\rangle_{n_2}\langle g|(b_n^\dagger b_n + c_n^\dagger b_n + b_n^\dagger c_n + c_n^\dagger c_n) \\
&+ \frac{g_3^2}{\Delta_3}|e\rangle_{n_3}\langle e|(c_n c_n^\dagger + c_n d_n^\dagger + d_n c_n^\dagger + d_n d_n^\dagger) \\
&- \frac{g_3^2}{\Delta_3}|g\rangle_{n_3}\langle g|(c_n^\dagger d_n + c_n^\dagger c_n + d_n^\dagger c_n + d_n^\dagger d_n) \\
&+ \frac{g_4^2}{\Delta_4}|e\rangle_{n_4}\langle e|(d_n d_n^\dagger + d_n a_{n+1}^\dagger + a_{n+1} d_n^\dagger + a_{n+1} a_{n+1}^\dagger) \\
&- \frac{g_4^2}{\Delta_4}|g\rangle_{n_4}\langle g|(d_n^\dagger d_n + a_{n+1}^\dagger d_n + d_n^\dagger a_{n+1} + a_{n+1}^\dagger a_{n+1}) \\
&+ \frac{g_a^2}{\Delta_a}(|e\rangle_{n_a}\langle e|a_n a_n^\dagger - |g\rangle_{n_a}\langle g|a_n^\dagger a_n) \\
&+ \frac{g_b^2}{\Delta_b}(|e\rangle_{n_b}\langle e|b_n b_n^\dagger - |g\rangle_{n_b}\langle g|b_n^\dagger b_n)
\end{aligned}
$$

$$+ \frac{g_c^2}{\Delta_c}(|e\rangle_{n_c}\langle e|c_n c_n^\dagger - |g\rangle_{n_c}\langle g|c_n^\dagger c_n)$$

$$+ \frac{g_d^2}{\Delta_d}(|e\rangle_{n_d}\langle e|d_n d_n^\dagger - |g\rangle_{n_d}\langle g|d_n^\dagger d_n)]. \tag{A4}$$

Assume that all the Xmon qubits are prepared in their ground states, and further combine the similar terms, then we can get Eq. (2).

APPENDIX B: THE DETECTING MATRIX

In the following, we show how to obtain the detecting matrix of the edge states. We solve the Lindblad master equation

$$\langle \dot{\rho}_j \rangle = -i\langle[H + H_d, \rho_j]\rangle + \kappa\langle L[\rho_n]\rho_j\rangle, \tag{B1}$$

where $L[\rho_n]\rho_j = \rho_n\rho_j\rho_n^\dagger - \{\rho_n^\dagger\rho_n, \rho_j\}/2$ is the Lindblad term and κ is the cavity decay rate. Then we can obtain

$$\langle \dot{a}_1 \rangle = -i\langle[H + H_d, a_1]\rangle + \kappa\left\langle a_n a_1 a_n^\dagger - \frac{\{a_n^\dagger a_n, a_1\}}{2}\right\rangle$$

$$= -i\langle[(\Delta_e - V\sin\theta)a_1^\dagger a_1 + \cos\varphi a_1^\dagger b_1 + \cos\varphi a_1 b_1^\dagger$$

$$+ \Omega_{1,a}a_1^\dagger + \Omega_{1,a}a_1, a_1]\rangle + \frac{\kappa}{2}\langle a_1\rangle$$

$$= -i\langle[(\Delta_e - V\sin\theta)a_1^\dagger a_1 + \cos\varphi a_1^\dagger b_1 + \Omega_{1,a}a_1^\dagger, a_1]\rangle$$

$$+ \frac{\kappa}{2}\langle a_1\rangle$$

$$= i\left(\Delta_e - V\sin\theta - \frac{i\kappa}{2}\right)\langle a_1\rangle + i\cos\varphi\langle b_1\rangle + i\Omega_{1,a}. \tag{B2}$$

Similarly, we also can get

$$\langle \dot{b}_1 \rangle = i\cos\varphi\langle a_1\rangle + i\left(\Delta_e - V\cos\theta - \frac{i\kappa}{2}\right)\langle b_1\rangle$$

$$+ i\sin\varphi\langle c_1\rangle + i\Omega_{1,b},$$

$$\langle \dot{c}_1 \rangle = i\sin\varphi\langle b_1\rangle + i\left(\Delta_e + V\sin\theta - \frac{i\kappa}{2}\right)\langle c_1\rangle$$

$$+ i\cos\varphi\langle d_1\rangle + i\Omega_{1,c},$$

$$\langle \dot{d}_1 \rangle = i\cos\varphi\langle c_1\rangle + i\left(\Delta_e + V\cos\theta - \frac{i\kappa}{2}\right)\langle d_1\rangle$$

$$+ i\sin\varphi\langle a_2\rangle + i\Omega_{1,d},$$

$$\cdots$$

$$\langle \dot{a}_n \rangle = i\sin\varphi\langle d_{n-1}\rangle + i\left(\Delta_e - V\sin\theta - \frac{i\kappa}{2}\right)\langle a_n\rangle$$

$$+ i\cos\varphi\langle b_n\rangle + i\Omega_{n,a},$$

$$\langle \dot{b}_n \rangle = i\cos\varphi\langle a_n\rangle + i\left(\Delta_e - V\cos\theta - \frac{i\kappa}{2}\right)\langle b_n\rangle$$

$$+ i\sin\varphi\langle c_n\rangle + i\Omega_{n,b},$$

$$\langle \dot{c}_n \rangle = i\sin\varphi\langle b_n\rangle + i\left(\Delta_e + V\sin\theta - \frac{i\kappa}{2}\right)\langle c_n\rangle$$

$$+ i\cos\varphi\langle d_n\rangle + i\Omega_{n,c},$$

$$\langle \dot{d}_n \rangle = i\cos\varphi\langle c_n\rangle + i\left(\Delta_e + V\cos\theta - \frac{i\kappa}{2}\right)\langle d_n\rangle + i\Omega_{n,d}. \tag{B3}$$

Under the steady-state solution $\langle \dot{\rho}_j \rangle = 0$, the expectation value of the cavity fields can be written as Eq. (10), and the matrix $\vec{T}_{4n,4n}$ satisfies

$$\vec{T}_{4n,4n} = \begin{bmatrix} -V\sin\theta & \cos\varphi & 0 & 0 & 0 & 0 & 0 & 0 \\ \cos\varphi & -V\cos\theta & \sin\varphi & 0 & 0 & 0 & 0 & 0 \\ 0 & \sin\varphi & V\sin\theta & \cos\varphi & 0 & 0 & 0 & 0 \\ 0 & 0 & \cos\varphi & V\cos\theta & \sin\varphi & 0 & 0 & 0 \\ 0 & 0 & 0 & \sin\varphi & -V\sin\theta & \cos\varphi & 0 & 0 \\ 0 & 0 & 0 & 0 & \cos\varphi & -V\cos\theta & \sin\varphi & 0 \\ 0 & 0 & 0 & 0 & 0 & \sin\varphi & V\sin\theta & \cos\varphi \\ 0 & 0 & 0 & 0 & 0 & 0 & \cos\varphi & V\cos\theta \\ & & & & & & & & \ddots \end{bmatrix}. \tag{B4}$$

[1] W. H. Zurek, U. Dorner, and P. Zoller, Dynamics of a Quantum Phase Transition, Phys. Rev. Lett. **95**, 105701 (2005).

[2] T. Tian, H. X. Yang, L. Y. Qiu, H. Y. Liang, Y. B. Yang, Y. Xu, and L. M. Duan, Observation of Dynamical Quantum Phase Transitions with Correspondence in an Excited State Phase Diagram, Phys. Rev. Lett. **124**, 043001 (2020).

[3] J. Ren, W. L. You, and A. M. Oleś, Quantum phase transitions in a spin-1 antiferromagnetic chain with long-range interactions and modulated single-ion anisotropy, Phys. Rev. B **102**, 024425 (2020).

[4] M. Z. Hasan and C. L. Kane, Colloquium: Topological insulators, Rev. Mod. Phys. **82**, 3045 (2010).

[5] X. L. Qi and S. C. Zhang, Topological insulators and superconductors, Rev. Mod. Phys. **83**, 1057 (2011).

[6] L. Qi, G. L. Wang, S. Liu, S. Zhang, and H. F. Wang, Dissipation-induced topological phase transition and periodic-driving-induced photonic topological state transfer in a small optomechanical lattice, Front. Phys. **16**, 12503 (2021).

[7] H. J. Zhang, C. X. Liu, X. L. Qi, X. Y. Deng, X. Dai, S. C. Zhang, and Z. Fang, Electronic structures and surface states

of the topological insulator Bi$_{1-x}$Sb$_x$, Phys. Rev. B **80**, 085307 (2009).

[8] A. A. Burkov and L. Balents, Weyl Semimetal in a Topological Insulator Multilayer, Phys. Rev. Lett. **107**, 127205 (2011).

[9] Y. Xia, D. Qian, D. Hsieh, L. Wray, A. Pal, H. Lin, A. Bansil, D. Grauer, Y. S. Hor, R. J. Cava, and M. Z. Hasan, Observation of a large-gap topological insulator class with a single Weyl cone on the surface, Nat. Phys. **5**, 398 (2009).

[10] M. C. Rechtsman, J. M. Zeuner, Y. Plotnik, Y. Lumer, D. Podolsky, F. Dreisow, S. Nolte, M. Segev, and A. Szameit, Photonic floquet topological insulators, Nature (London) **496**, 196 (2013).

[11] J. Cao, X. X. Yi, and H. F. Wang, Band structure and the exceptional ring in a two-dimensional superconducting circuit lattice, Phys. Rev. A **102**, 032619 (2020).

[12] M. Y. Han, B. Özyilmaz, Y. Zhang, and P. Kim, Energy Band-Gap Engineering of Graphene Nanoribbons, Phys. Rev. Lett. **98**, 206805 (2007).

[13] A. P. Schnyder, S. Ryu, A. Furusaki, and A. W. W. Ludwig, Classification of topological insulators and superconductors in three spatial dimensions, Phys. Rev. B **78**, 195125 (2008).

[14] W. Al-Sawai, H. Lin, R. S. Markiewicz, L. A. Wray, Y. Xia, S. Y. Xu, M. Z. Hasan, and A. Bansil, Topological electronic structure in half-Heusler topological insulators, Phys. Rev. B **82**, 125208 (2010).

[15] R. J. Cava, H. Ji, M. K. Fuccillo, Q. D. Gibson, and Y. S. Hor, Crystal structure and chemistry of topological insulators, J. Mater. Chem. C **1**, 3176 (2013).

[16] Y. Xing, L. Qi, J. Cao, D. Y. Wang, C. H. Bai, H. F. Wang, A. D. Zhu, and S. Zhang, Controllable photonic and phononic edge localization via optomechanically induced kitaev phase, Opt. Express **26**, 16250 (2018).

[17] K. M. Dantscher, D. A. Kozlov, P. Olbrich, C. Zoth, P. Faltermeier, M. Lindner, G. V. Budkin, S. A. Tarasenko, V. V. Bel'kov, Z. D. Kvon, N. N. Mikhailov, S. A. Dvoretsky, D. Weiss, B. Jenichen, and S. D. Ganichev, Cyclotron-resonance-assisted photocurrents in surface states of a three-dimensional topological insulator based on a strained high-mobility HgTe film, Phys. Rev. B **92**, 165314 (2015).

[18] J. T. Shen and S. Fan, Coherent Single Photon Transport in a One-Dimensional Waveguide Coupled with Superconducting Quantum Bits, Phys. Rev. Lett. **95**, 213001 (2005).

[19] Y. Yan, L. Qi, D. Y. Wang, Y. Xing, H. F. Wang, and S. Zhang, Topological phase transition and phase diagrams in a two-leg Kitaev ladder system, Ann. Phys. (Berlin, Ger.) **532**, 1900479 (2020).

[20] W. X. Cui, L. Qi, Y. Xing, S. Liu, S. Zhang, and H. F. Wang, Topological and nontopological photonic states in two coupled circuit quantum electrodynamics chains, Laser Phys. Lett. **17**, 055206 (2020).

[21] F. Mei, J. B. You, W. Nie, R. Fazio, S. L. Zhu, and L. C. Kwek, Simulation and detection of photonic chern insulators in a one-dimensional circuit-QED lattice, Phys. Rev. A **92**, 041805 (2015).

[22] L. Qi, Y. Xing, J. Cao, X. X. Jiang, C. S. An, A. D. Zhu, S. Zhang, and H. F. Wang, Simulation and detection of the topological properties of a modulated Rice-Mele model in a one-dimensional circuit-QED lattice, Sci. China: Phys., Mech. Astron. **61**, 080313 (2018).

[23] L. Xiang, Z. Zong, Z. Sun, Z. Zhan, Y. Fei, Z. Dong, C. Run, Z. Jia, P. Duan, J. Wu, Y. Yin, and G. Guo, Simultaneous Feedback and Feedforward Control and Its Application to Realize a Random Walk on the Bloch Sphere in an Xmon-Superconducting-Qubit System, Phys. Rev. Applied **14**, 014099 (2020).

[24] F. Mei, Z. Y. Xue, D. W. Zhang, L. Tian, C. Lee, and S. L. Zhu, Witnessing topological Weyl semimetal phase in a minimal circuit-QED lattice, Quantum Sci. Technol. **1**, 015006 (2016).

[25] I. C. Hoi, C. M. Wilson, G. Johansson, J. Lindkvist, B. Peropadre, T. Palomaki, and P. Delsing, Microwave quantum optics with an artificial atom in one-dimensional open space, New J. Phys. **15**, 025011 (2013).

[26] W. Tan, L. Chen, X. Ji, and H. Q. Lin, Photonic simulation of topological superconductor edge state and zero-energy mode at a vortex, Sci. Rep. **4**, 7381 (2014).

[27] P. Barthelemy and L. M. K. Vandersypen, Quantum dot systems: A versatile platform for quantum simulations, Ann. Phys. (Berlin, Ger.) **525**, 808 (2013).

[28] L. Qi, Y. Xing, G. L. Wang, S. Liu, S. Zhang, and H. F. Wang, Topological phase induced by distinguishing parameter regimes in a cavity optomechanical system with multiple mechanical resonators, Phys. Rev. A **101**, 052325 (2020).

[29] M. Kurzyna and T. Kwapiński, Edge-state dynamics in coupled topological chains, Phys. Rev. B **102**, 195429 (2020).

[30] K. Wang, G. Hu, R. Liu, Y. Zhang, M. Dan, L. Li, and Y. Zhang, Polarization-Driven Edge-State Transport in Transition-Metal Dichalcogenides, Phys. Rev. Applied **13**, 054074 (2020).

[31] F. Grusdt, M. Höning, and M. Fleischhauer, Topological Edge States in the One-Dimensional Superlattice Bose-Hubbard Model, Phys. Rev. Lett. **110**, 260405 (2013).

[32] Y. E. Kraus, Y. Lahini, Z. Ringel, M. Verbin, and O. Zilberberg, Topological States and Adiabatic Pumping in Quasicrystals, Phys. Rev. Lett. **109**, 106402 (2012).

[33] C. Si, J. Liu, Y. Xu, J. Wu, B. L. Gu, and W. Duan, Functionalized germanene as a prototype of large-gap two-dimensional topological insulators, Phys. Rev. B **89**, 115429 (2014).

[34] H. Huang, Y. Xu, J. Wang, and W. Duan, Emerging topological states in quasi-two-dimensional materials, WIREs: Comput. Mol. Sci. **7**, e1296 (2017).

[35] L. Kou, B. Yan, F. Hu, S. C. Wu, T. O. Wehling, C. Felser, C. Chen, and T. Frauenheim, Graphene-based topological insulator with an intrinsic bulk band gap above room temperature, Nano Lett. **13**, 6251 (2013).

[36] Y. Ren, Z. Qiao, and Q. Niu, Topological phases in two-dimensional materials: a review, Rep. Prog. Phys. **79**, 066501 (2016).

[37] C. Yin, L. Li, and S. Chen, Transition from a nodal-loop phase to a nodal-chain phase in a periodicically modulated optical lattice, Phys. Rev. A **97**, 013604 (2018).

[38] L. Qi, Y. Xing, G. L. Wang, S. Liu, S. Zhang, and H. F. Wang, Topological and nontopological edge states induced by qubit-assisted coupling potentials, Ann. Phys. (Berlin, Ger.) **532**, 2000067 (2020).

[39] A. B. Khanikaev, S. Hossein Mousavi, W. K. Tse, M. Kargarian, A. H. MacDonald, and G. Shvets, Photonic topological insulators, Nat. Mater. **12**, 233 (2013).